

Highly efficient bifacial semitransparent perovskite solar cells based on molecular doping of CuSCN hole transport layer

Shixin Hou(侯世欣), Biao Shi(石标), Pengyang Wang(王鹏阳), Yucheng Li(李玉成), Jie Zhang(张杰), Peirun Chen(陈沛润), Bingbing Chen(陈兵兵), Fuhua Hou(侯福华), Qian Huang(黄茜), Yi Ding(丁毅), Yuelong Li(李跃龙), Dekun Zhang(张德坤), Shengzhi Xu(许盛之), Ying Zhao(赵颖), Xiaodan Zhang(张晓丹)

Citation: Chin. Phys. B . 2020, 29(7): 078801 . **doi:** 10.1088/1674-1056/ab99ae
Journal homepage: http://cpb.iphy.ac.cn; http://iopscience.iop.org/cpb

What follows is a list of articles you may be interested in

Effect of carrier mobility on performance of perovskite solar cells

Yi-Fan Gu(顾一帆), Hui-Jing Du(杜会静), Nan-Nan Li(李楠楠), Lei Yang(杨蕾), Chun-Yu Zhou(周春宇)

Chin. Phys. B . 2019, 28(4): 048802 . **doi:** 10.1088/1674-1056/28/4/048802

Two-step processed efficient perovskite solar cells via improving perovskite/PTAA interface using solvent engineering in PbI_2 precursor

Cao-Yu Long(龙操玉), Ning Wang(王宁), Ke-Qing Huang(黄可卿), Heng-Yue Li(李恒月), Biao Liu(刘标), Jun-Liang Yang(阳军亮)

Chin. Phys. B . 2020, 29(4): 048801 . **doi:** 10.1088/1674-1056/ab7744

TiO_2 composite electron transport layers for planar perovskite solar cells by mixed spray pyrolysis with precursor solution incorporating TiO_2 nanoparticles

Jiaqi Tian(田嘉琪), Hongcui Li(李红翠), Haiyue Wang(王海月), Bo Zheng(郑博), Yebin Xue(薛叶斌), Xizhe Liu(刘喜哲)

Chin. Phys. B . 2018, 27(1): 018810 . **doi:** 10.1088/1674-1056/27/1/018810

Promise of commercialization: Carbon materials for low-cost perovskite solar cells

Yu Cai(蔡宇), Lusheng Liang(梁禄生), Peng Gao(高鹏)

Chin. Phys. B . 2018, 27(1): 018805 . **doi:** 10.1088/1674-1056/27/1/018805

420 nm thick $CH_3NH_3PbI_{3-x}Br_x$ capping layers for efficient TiO_2 nanorod array perovskite solar cells

Long Li(李龙), Cheng-Wu Shi(史成武), Xin-Lian Deng(邓新莲), Yan-Qing Wang(王艳青), Guan-Nan Xiao(肖冠南), Ling-Ling Ni(倪玲玲)

Chin. Phys. B . 2018, 27(1): 018804 . **doi:** 10.1088/1674-1056/27/1/018804

Highly efficient bifacial semitransparent perovskite solar cells based on molecular doping of CuSCN hole transport layer*

Shixin Hou(侯世欣)[1,2,3,4,5], Biao Shi(石标)[1,2,3,4,5], Pengyang Wang(王鹏阳)[1,2,3,4,5,†], Yucheng Li(李玉成)[1,2,3,4,5], Jie Zhang(张杰)[1,2,3,4,5], Peirun Chen(陈沛润)[1,2,3,4,5], Bingbing Chen(陈兵兵)[1,2,3,4,5], Fuhua Hou(侯福华)[1,2,3,4,5], Qian Huang(黄茜)[1,2,3,4,5], Yi Ding(丁毅)[1,2,3,4,5], Yuelong Li(李跃龙)[1,2,3,4,5], Dekun Zhang(张德坤)[1,2,3,4,5], Shengzhi Xu(许盛之)[1,2,3,4,5], Ying Zhao(赵颖)[1,2,3,4,5], and Xiaodan Zhang(张晓丹)[1,2,3,4,5,‡]

[1] *Institute of Photoelectronic Thin Film Devices and Technology of Nankai University, Tianjin* 300350, *China*
[2] *Key Laboratory of Photoelectronic Thin Film Devices and Technology of Tianjin, Tianjin* 300350, *China*
[3] *Collaborative Innovation Center of Chemical Science and Engineering (Tianjin), Tianjin* 300072, *China*
[4] *Renewable Energy Conversion and Storage Center of Nankai University, Tianjin* 300072, *China*
[5] *Engineering Research Center of Thin Film Photoelectronic Technology, Ministry of Education, Tianjin* 300350, *China*

(Received 5 February 2020; revised manuscript received 19 May 2020; accepted manuscript online 5 June 2020)

Coper thiocyanate (CuSCN) is generally considered as a very hopeful inorganic hole transport material (HTM) in semitransparent perovskite solar cells (ST-PSCs) because of its low parasitic absorption, high inherent stability, and low cost. However, the poor electrical conductivity and low work function of CuSCN lead to the insufficient hole extraction and large open-circuit voltage loss. Here, 2,3,5,6-tetrafluoro-7,7,8,8-tetracyanoquinodimethane (F4TCNQ) is employed to improve conductivity of CuSCN and band alignment at the CuSCN/perovskite (PVK) interface. As a result, the average power conversion efficiency (PCE) of PSCs is boosted by ≈ 11%. In addition, benefiting from the superior transparency of p-type CuSCN HTMs, the prepared bifacial semitransparent n–i–p planar PSCs demonstrate a maximum efficiency of 14.8% and 12.5% by the illumination from the front side and back side, respectively. We believe that this developed CuSCN-based ST-PSCs will promote practical applications in building integrated photovoltaics and tandem solar cells.

Keywords: perovskite solar cell, CuSCN, inorganic hole transport layer, organic doping, semitransparent solar cell

PACS: 88.40.H–, 88.40.hj **DOI:** 10.1088/1674-1056/ab99ae

1. Introduction

Expanding application fields and improving power conversion efficiency (PCE) of solar cells have become inescapable issues to further promote the development of photovoltaic (PV) market. Semitransparent solar cells (ST-SCs) provide an attractive choice to address aforementioned problems, and thus receive overwhelming attention. For example, ST-SCs can be utilized not only as color-tunable building integrated PV (BIPV),[1] wearable electronics,[2] and PV vehicles[3] to excite future applications, but also as subcell of multi-junction[4] or bifacial PV devices[5] to convert more solar energy into electricity, and therefore improve PCE. Organic–inorganic hybrid perovskite solar cells (PSCs) have emerged as a promising candidate for ST-SCs, because opaque PSCs have achieved PCE of 25.2%[6] with unprecedented speed attributing to its direct band gap, high absorption coefficient, low exciton binding energy, and a long electron–hole diffusion length. Simple device architecture, facile fabrication process, and higher PCE make the planar heterojunction stand out from all PSCs device structures, especially the planar n–i–p device.[7–9] Different from opaque solar cells, both charge collection efficiency and light transmittance of HTMs are vital to avoid influencing light absorption in perovskite active layer and realize high performance of ST-PSCs.[10] Generally, 2,2',7,7'-tetrakis (N,N-di-p-Methoxyphenylamine)-9, 9'-spirobifluorene (Spiro-OMeTAD)[11] or poly (triarylamine) (PTAA)[12] are used as HTMs in most efficient PSCs. Unfortunately, both of them are unstable and expensive, which will greatly affect their wide application in the future. Besides, the serious light absorption in short-wavelength range is also harmful to light harvesting of perovskite absorption layer. Therefore, it is urgent and essential to explore alternative HTMs.[13]

Recently, copper thiocyanate (CuSCN) is paid much attention due to its excellent material stability, extremely low price, and compatible HOMO (highest occupied molecular orbited) level with perovskite. And it is noteworthy that the hole mobility of CuSCN of 0.01 $cm^2 \cdot V^{-1} \cdot s^{-1}$–0.1 $cm^2 \cdot V^{-1} \cdot s^{-1}$ is remarkably higher than that of common organic HTMs, such

*Project supported by the National Key Research and Development Program of China (Grant No. 2018YFB1500103), the National Natural Science Foundation of China (Grant No. 61674084), the Overseas Expertise Introduction Project for Discipline Innovation of Higher Education of China (Grant No. B16027), and the Science and Technology Project of Tianjin, China (Grant No. 18ZXJMTG00220).

†Corresponding author. E-mail: pywang@nankai.edu.cn
‡Corresponding author. E-mail: xdzhang@nankai.edu.cn

© 2020 Chinese Physical Society and IOP Publishing Ltd

as 10^{-3} $cm^2 \cdot V^{-1} \cdot s^{-1}$ of PTAA and 4×10^{-5} $cm^2 \cdot V^{-1} \cdot s^{-1}$ of Spiro-OMeTAD.[14] A report of the PSCs based opaque CuSCN with PCE over 20%[15] confirmed that CuSCN can be employed as excellent HTM. In addition, the low parasitic absorption also allows it as potential candidate of HTMs for ST-PSCs. For instance, Jen and co-authors[16] adopted CuSCN as HTM instead of PEDOT:PSS to prepare ST-PSCs to obtain PCE of 10% and average visible transmittance (AVT) of 25%. Fan and co-authors[17] fabricated bifacial semitransparent n–i–p planar PSCs, which achieved a maximum efficiency of 12.47% and 8.74% by illumination from the front side and back side, respectively. Wang and co-authors[18] used the CuSCN and ITO as the HTMs and back electrode in the PSCs, respectively. Compared with the Spiro-OMeTAD based ST-PSCs, the CuSCN-based ST-PSCs exhibited higher PCE of 14.2% and 13.3% by illumination from the front side and back side, respectively. Despite many efforts have been made in employing CuSCN as HTM, few attentions were focused on the poor electrical conductivity and small work function of CuSCN. Those problems will cause weak built-in field within limited film thickness, and at the same time cause energy level offset at the CuSCN/perovskite interface.[19] Consequently, it can be deduced that there will be a large amount of hole accumulation and electron–hole recombination at the interface of CuSCN/perovskite due to the low holes transfer efficiency of intrinsic CuSCN.

In this work, F4TCNQ was doped into CuSCN to be used as the HTM in CsFAMA based n–i–p planar perovskite solar cells, which optimize the energy level alignment at the I/P interface in order to achieve better hole transport. Ultraviolet photoelectron spectroscopy (UPS) and x-ray photoelectron spectroscopy (XPS) indicated that, after F4TCNQ doping, the energy level positions of CuSCN HTMs changed, in which Fermi level (E_F) decreased from -4.82 eV to -4.90 eV and valence band maximum (VBM) $-E_F$ decreased from 0.71 eV to 0.68 eV. Therefore, the average conversion efficiency of CsFAMA mixed cation PSCs was improved by about 11%, and a PCE of 16.6% for a champion cell. In addition, for bifacial semitransparent n–i–p planar PSC using CuSCN as HTM, maximum PCE of 14.8% and 12.5% were achieved by illuminated from the front side and the rear side, respectively.

2. Experiments

2.1. Materials

Lead bromide ($PbBr_2$, 99.99%), copper thiocyanate (CuSCN, 99%), cesium iodide (CsI, 99.999%), chlorobenzene (CB, 99.8%), dimethylformamide (DMF, 99.9%), and dimethyl sulfoxide (DMSO, 99.9%) were purchased from Sigma-Aldrich. Tin(IV) oxide colloid precursor (15% in H_2O colloidal) was purchased from Alfa Aesar. F4TCNQ (99%) were purchased from materwin. Lead iodide (PbI_2, 99.99%), formamidinium iodide (FAI), and methylammonium bromide (MABr) wear purchased from Xi'an Polymer Light Technology Corp. Diethyl sulfide (DES, 98%) was purchased from Shanghai TCI.

2.2. Fabrication of devices

ITO glass substrates were cleaned with detergent, deionized water, acetone, and isopropanol for 30 min each time. The previously cleaned ITO glass substrates were exposed to ultraviolet light at room temperature for 10 min, spin coated SnO_2 layer at 4000 rpm for 30 s then annealed at 150 °C for 30 min in ambient air. The CsFAMA mixed precursor solution was prepared in a glove box. Precursor solution of perovskite was prepared by mixing PbI_2 (548.62 mg), $PbBr_2$ (57.06 mg), FAI (178.94 mg), MABr (17.41 mg), CsI (27.04 mg) in DMF/DMSO (V/V 780 μl/220 μl). Subsequently, perovskite films were prepared by spin coating in a two-step programme at 1000 rpm and 5000 rpm for 10 s and 30 s. During the second step, 100 μl of chlorobenzene was dropped on the spinning substrate 10 s prior to the end of the programme and finally annealed on a hot plate at 130 °C in a glove box for 20 min.

The F4TCNQ was dissolved in chlorobenzene at the concentration of 1 mg/ml and added it in CuSCN(30 mg/ml, DES) solution at a volume ratio of 1%, 3%, 5%, and 7%, respectively. Doped-CuSCN and undoped-CuSCN layers were spin-coated on the ITO/SnO_2/CsFAMA substrates at the speed of 4000 rpm for 30 s. Drying was performed at room temperature for 10 min, and then it was annealed at 80 °C for 5 min to form the CuSCN films. MoO_X with thickness of 9 nm was thermally evaporated in high vacuum of 1×10^{-4} Pa, and grew at a slow rate of 0.1 Å/s, while the substrate temperature was kept at room temperature. Then ITO with thickness of 100 nm was deposited at room temperature by DC magnetron sputter deposition. Finally, gold grid electrode with thickness of 100 nm was deposited by thermal evaporation on the top.

2.3. Characterization

X-ray photoelectron spectroscopy (XPS) was carried out on a Thermo VG ESCALAB 250X with Al Ka radiation as excitation source, and used the C 1s neutral carbon peak at 284.8 eV to calibrate the binding energy. Ultraviolet photoelectron spectroscopy (UPS) with a VG Scienta R4000 analyzer and using a monochromatic He I light source (21.22 eV) was used to characterize the molecular energy levels. Secondary electron cutoff (SEC) was observed with a sample bias of -5 V. The method to determine the work function (ϕ) was based on the difference between the photon energy and the binding energy of the secondary cutoff edge. Scanning electron microscope (SEM, FEI NanoSEM650) was

used to measure the surface morphology of undoped and doped CuSCN. In addition, surface roughness of undoped and doped CuSCN was characterized by atomic force microscope (AFM, NanoNavi-SPA400). The transmittance and absorbance of undoped and doped CuSCN were characterized with a UV–vis-NIR spectrophotometer (Cary 5000, VARIAN). A fluorescence spectrophotometer (Edinburgh Instruments, FLS 980) was used to record room temperature steady-state photoluminescence (PL) and time-resolved photoluminescence (TRPL). The photocurrent density–voltage (J–V) curves of devices were measured under one sun illumination by using a Keithley 2400 digital source meter. The dark current density (ITO/SnO_2/PVK/HTM/Au) and trap state density (ITO/HTM/PVK/HTM/Au) were both examined by Keithley 2400 digital source meter under dark condition. External quantum efficiency (EQE) spectrum was obtained without any voltage bias in the case where the EQE system (QEX10, PV Measurement Co, Ltd.) was used in the DC mode.

3. Results and discussion

The device schematic diagram of the undoped and doped CuSCN are illustrated in Fig. 1(a). At present, in order to enhance the characteristics of hole transport layers, lots of strategies were conducted,[20–22] such as He and coauthors[23] found that Cu doping NiO results in increased work function and better energy levels alignment with enhanced device performance; Liao and coauthors[24] proved that the incorporation of copper salts achieved a p-type doping with efficient charge transfer complex, which resulted in improved film conductivity and hole mobility in spiro-OMeTAD:copper salts composite films. As a result, the PCE is largely improved from 14.82% to 18.02%. There are many methods to control the carrier concentrations in HTMs, and doping is one of the most effective methods.[25,26] Strong electron acceptor of F4TCNQ can be easily ionized by attracting electrons.[27] With the measurement of UV–vis absorption spectroscopy, the optical bandgap values of undoped CuSCN and doped CuSCN are determined to be 3.66 eV and 3.67 eV, respectively (see Fig. A1 in Appendix A). To explore the mechanism, electronic structures of CuSCN with and without F4TCNQ are probed with UPS.[28] As shown in Fig A2(a), the valance band spectra show that after doping F4TCNQ, the difference between E_F and VBM of CuSCN narrows from 0.71 eV to 0.68 eV, indicating the hole concentration is enhanced. From the UPS measurement, the work functions (ϕ) of the undoped and doped CuSCN are calculated to be 4.82 eV and 4.90 eV, respectively (see Fig. A2(b)). The VBM of the doped CuSCN (5.58 eV) went deeper than undoped CuSCN (5.53 eV) as referred to vacuum level. From this result, we can draw the conclusion that the transferring of electrons from CuSCN to F4TCNQ was successful, which is consistent with some reports of F4TCNQ.[29] The negative shifts of E_F and VBM effectively reduce the energy level offset between CuSCN and perovskite absorbers and enhance built-in field strength, and hence improve the device performance. From the XPS measurements, the Cu 2p core level peaks have unambiguous shifts about 0.2 eV after doping F4TCNQ (Fig A3), and the core level peaks of S 2p, C 1s, and N 1s also have unambiguous shifts about 0.1 eV–0.4 eV after doping F4TCNQ (Fig. A3) respectively, which further make us confirm that electron transfer from CuSCN to F4TCNQ happens.[30]

Based on the aforementioned problem, the band diagram of the CuSCN/perovskite in the PSCs is shown in Fig. 1(b) and the corresponding band bending at CuSCN-perovskite interface of before and after doping F4TCNQ is shown in Figs. A2(c) and A2(d), where the VBM and E_F of CsFAMA perovskite is set at 5.65 eV and at the middle of the band gap, respectively.[23,31] It can be clearly seen that the energy level offset between CuSCN VBM and perovskite VBM for charge transfer is decreased from 0.12 eV to 0.07 eV. Owing to the simultaneous reduction of its work function, the band bending of CuSCN/perovskite interface was enlarged 0.08 eV, doped CuSCN/PVK interface present accelerated charge transfer and reduces holes accumulation, resulting in lower charge recombination and higher charge transport efficiency from perovskite.

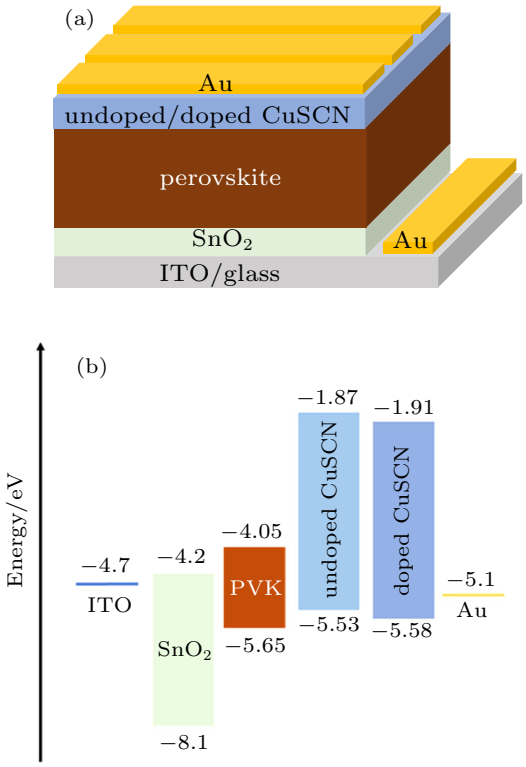


Fig. 1. (a) Schematic device architecture. (b) The energy band structure diagram of PSCs.

Steady-state photoluminescence (PL) and time-resolved photoluminescence (TRPL) decay measurements are used to

understand the hole extraction capability and recombination characteristics of the devices with different HTMs. As shown in Fig. 2(a), for the doped CuSCN, a stronger quenching effect is observed, indicating an enhanced hole extraction capability. The measurement of TRPL can detect the time intensity change of radiative processes. The TRPL decay can be ascribed to the perovskite bulk radiative or nonradiative recombination of electrons and holes, charge capture at the surface defects of perovskite surface, or the transfer of hole from perovskite to HTM. The measured TRPL curves are shown in Fig. 2(b). Fitting with exponential, results are shown as equation as follows:

$$Y = A_1 \exp(-t/\tau_1) + A_2 \exp(-t/\tau_2) + Y_0, \tag{1}$$

where A_1 and A_2 are the corresponding decay amplitudes, τ_1 is the fast decay time about interface recombination, and τ_2 is the slow decay time reflected the bulk recombination, Y_0 is a constant for the baseline offset.[32] The obtained parameters for the TRPL data are listed in Table A1 in Appendix A. The better energy level structure makes PL quenching faster, which shows that the ability of carrier extraction is improved. Meanwhile, it is very important to reduce carrier recombination to improve the PCE of device.[33]

The dark current–voltage (J–V) characteristics of hole-only devices based on ITO/NiO_x/perovskite/undoped or doped CuSCN/Au were used to evaluate carrier recombination at the interface of CuSCN/Perovskite. The space-charge-limited currents (SCLC) curves is used to measure the trap state density state (n_{trap}). As shown in Figs. 2(c) and 2(d), the dark J–V curve can be divided into three parts. In the case where the applied voltage is higher than the voltage at the first kink point ($n > 3$), it can be concluded that all the trap states are filled with injected carriers, because the current exhibits a rapid nonlinear growth state. The applied voltage at the kink point is the trap-filled limit voltage (V_{TFL}) defined by the trap state density[34]

$$V_{TEL} = \frac{e n_{trap} d^2}{2\varepsilon\varepsilon_0}, \tag{2}$$

where d and ε are the thickness and relative dielectric constant of perovskite film, and ε_0 is the constant of permittivity in free space. The V_{TFL} is linearly related to the n trap. As shown in Figs. 2(c) and 2(d), the V_{TFL} are 1.36 V and 1.12 V for undoped and doped devices, respectively. Lower V_{TFL} represents the less carrier recombination at the interface of CuSCN/perovskite. This further indicates that the doped CuSCN has a faster charge transfer capability, thereby obtaining faster charge extraction, reducing the accumulation of charge at the interface and charge recombination in the bulk.[35]

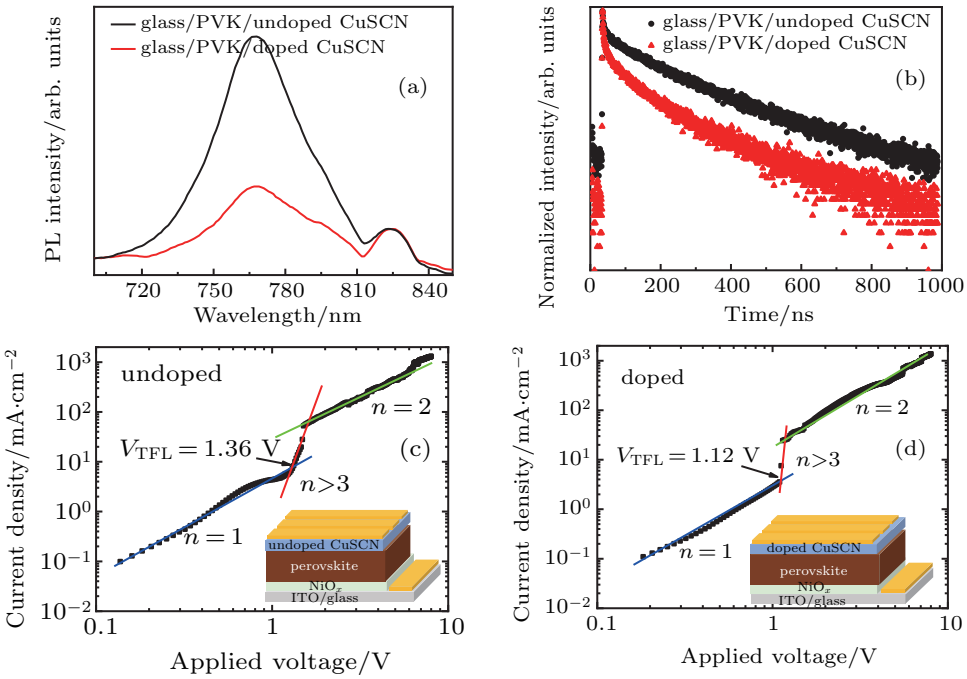


Fig. 2. Steady-state (a) and time-resolved (b) photoluminescence of glass/perovskite/CuSCN and glass/perovskite/F4TCNQ-doped CuSCN; SCLC of (c) ITO/NiO_x/PVK/F4TCNQ-undoped CuSCN/Au, and (d) ITO/NiO_x/PVK/F4TCNQ-doped CuSCN/Au.

The photovoltaic performance of the CsFAMA perovskite PSCs with undoped and doped CuSCN HTMs is analyzed and is shown in Fig. 3. It can be seen that the cell based on doped CuSCN achieves a considerably higher short-circuit current density (J_{sc}), open-circuit voltage (V_{oc}), and fill factor (FF) and thus higher PCE. The results of the J–V curves of the best devices indicate that using F4TCNQ-doped CuSCN as HTMs can significantly improve device performance (Fig. 3(a)). Finally, the champion cell with PCE of 16.6% is obtained, while the undoped device achieves an optimal PCE of 13.5%. Ta-

ble 1 summarizes all photovoltaic parameters. The EQE spectra are shown in Fig. 3(b). Devices using doped CuSCN as HTMs in the range from 300 nm to 800 nm have higher EQE values compared to reference devices, which indicates that doped CuSCN has stronger charge extraction and transporting capabilities. The photocurrents of the undoped and doped CuSCN based solar cells calculated from the results of EQE are 19.5 mA/cm^2 and 20.3 mA/cm^2, respectively.

The long-term stability of these PSCs can also be evaluated by the *J*–*V* characteristics monitoring of the devices stored in glove box (RH < 10%) at room temperature. As shown in Fig. 3(c), after 200 days, 88% of the initial PCE remains for the doped CuSCN, while only 76% remains for the undoped CuSCN. And we also conducted experiments about the steady-state PCEs for the devices with and without doping, which are 16.5% and 13.2%, respectively (Fig. A6). The 3% F4TCNQ is an optimal doping ratio (Fig. A4 and Table A2 in Appendix A), the statistics performances for 25 devices with 3% F4TCNQ doped or undoped devices are presented in Fig. 3(d) and Fig. A5. The averaged PCE for undoped devices is 13.1%, about 8.5% lower than that of the devices with F4TCNQ-doping (14.5%). From these results, the most important improvement is that V_{oc} increases from 1.06 V to 1.10 V (Fig. A7). In addition, after using F4TCNQ-doped CuSCN as HTMs, the series resistance (R_s) of device decreases, and the shunt resistance (R_{sh}) increases (Table 1). The increase of V_{oc} and FF means that the recombination at the CuSCN/perovskite interface can be reduced by doped CuSCN. The current–voltage curves measured under both reverse and forward scan directions were shown in Fig. A6, the parameters of the devices as shown in Table 1. And we also calculated the *J*–*V* hysteresis factor, which defined by $(PCE_{Reverse} - PCE_{Forward})/PCE_{Reverse}$,[36–38] the hysteresis factor of the champion PSCs based on doped and undoped CuSCN are 0.030 and 0.036, respectively. Both devices with negligible hysteresis (Fig. A7 and Table 1).

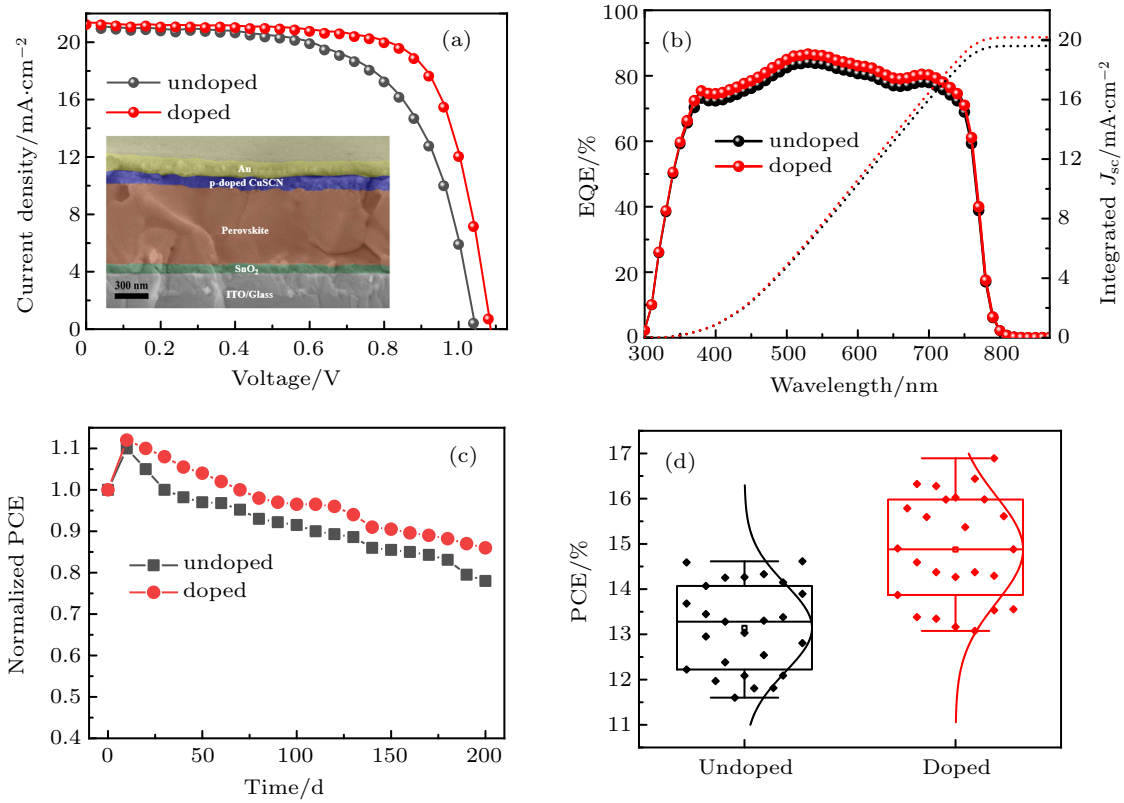


Fig. 3. (a) *J*–*V* curves from forward-biased (FB) to short-circuit (SC) of the optimal CsFAMA PSCs using CuSCN or F4TCNQ-doped CuSCN as HTMs under 1-sun illumination. The insert is the cross-sectional scanning electron microscope image of PSCs; (b) EQE and integrated J_{sc} spectra of the corresponding optimal devices. (c) Normalized PCE of PSC (undoped CuSCN and doped CuSCN) as a function of aging time at 25 °C in N_2 atmosphere. (d) Statistics of PCE for CuSCN and F4TCNQ-doped CuSCN devices (25 cells are included).

Table 1. Summary of photovoltaic parameters of n–i–p planar PSCs based on doped and undoped CuSCN HTMs.

	Devices scan direction	J_{sc}/(mA/cm^2)	V_{oc}/V	FF/%	PCE/%	R_s/(Ω /cm^2)	R_{sh}/(kΩ /cm^2)
Undoped CuSCN	reverse	20.1	1.06	61.3	13.1	8.6	2.3
	forward	20.3	1.06	63.1	13.5	8.2	2.4
Doped CuSCN	reverse	21.1	1.10	68.8	16.0	5.1	4.6
	forward	21.5	1.10	70.5	16.6	4.5	4.9

As depicted in Fig. 4(a), compared with the reference device, the dark current density of the device with doped CuSCN is about one order of magnitude lower. This shows that using doped CuSCN as HTM can effectively inhibit the leakage current density of perovskite. Therefore, photo-generated carriers are dissociated effectively in the photovoltaic process. In addition, according to Eq. (3), V_{oc} can be increased by reducing the leakage current density[39]

$$V_{oc} = \left(\frac{nRT}{F}\right) \ln\left[\frac{J_{sc}}{J_0} - 1\right] = \left(\frac{nRT}{F}\right) \ln\left(\frac{J_{sc}}{J_0}\right), \quad (3)$$

where n is the ideal factor, R and F are the ideal gas and Faraday constants, respectively, T is the temperature, J_{sc} is the short circuit current, and J_0 is the dark current. It can be seen that the V_{oc} increases with the decrease of the leakage current, thus devices with the doped hole transport material can obtain higher J_{sc} and V_{oc} values. Actually, the atomic force microscopy (AFM) images indicate that the root-mean-square roughness (RMS) is reduced from 39 nm to 23 nm after doping (see Figs. 4(b)–4(e)), which means that the smoother and denser hole transport layer may prevent direct contact between perovskite and gold electrode. All of these will reduce carrier recombination loss, and then increases the V_{oc} of the device.

The vertical conductivity of the undoped and doped film are measured by J–V test system. Figure 4(f) shows that the conductivity of the doped CuSCN film is 2.51×10^{-4} S/cm, which is almost 2 times higher than the undoped CuSCN film (1.48×10^{-4} S/cm). The improvement of the conductivity of the HTM film will lead to the reduction of the R_s, thus improving the charge collection efficiency meanwhile improving the fill factor.[40]

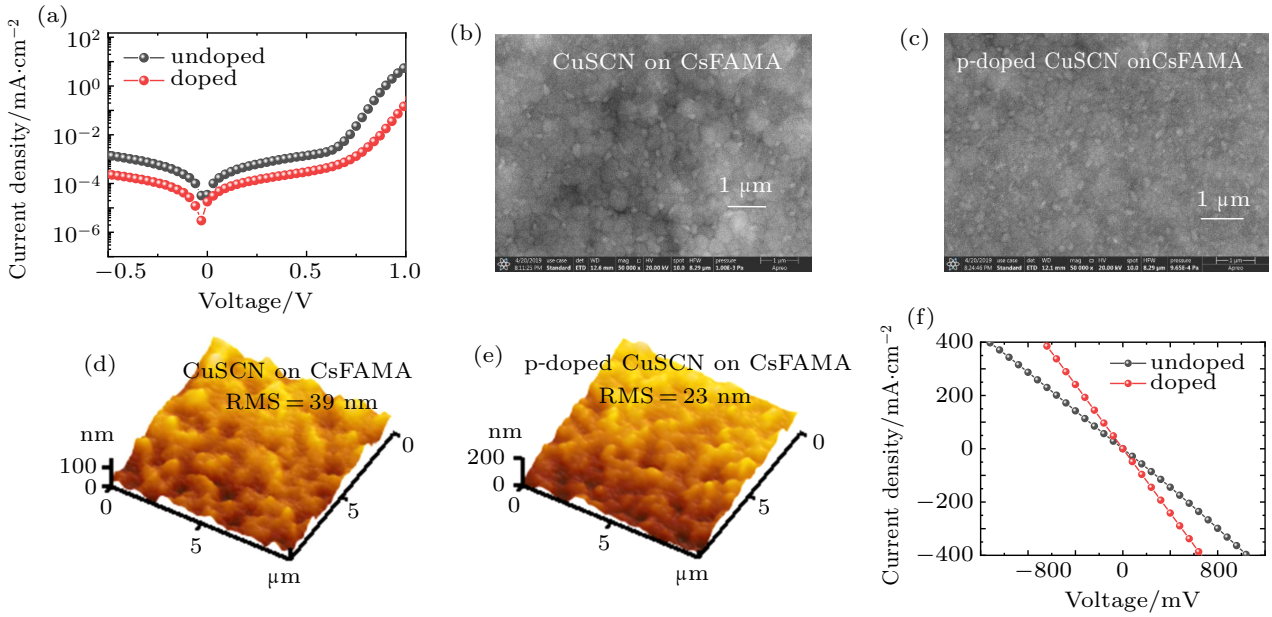


Fig. 4. (a) Dark J–V curves of PSCs with CuSCN or F4TCNQ-doped CuSCN; SEM [(b) and (c)] and AFM [(d) and (e)] topographic images of CuSCN and F4TCNQ-doped CuSCN on the CsFAMA perovskite films. The scale bar is 1 μm for each SEM image and the scan scale is 10 μm×10 μm for AFM images. (f) Current–voltage curves of CuSCN and F4TCNQ-doped CuSCN thin films.

As shown in Fig. 5(a), the p-type CuSCN HTM shows excellent transparency throughout the entire UV–vis–NIR range. In addition, the F4TCNQ-doped CuSCN demonstrates almost equivalent transmittance compared with undoped sample. This high transparency ensures that the perovskite absorption layer will have enough light under illumination from HTL side, and thus potentially leads to higher photocurrent in n–i–p ST-PSCs. Accordingly, the wide bandgap CuSCN ($E_g = 3.67$ eV) may be used as an excellent transparent HTM, applied on the bifacial ST-PSCs. Figure 5(b) shows the structure of a bifacial semitransparent n–i–p planar PSCs: ITO-glass/SnO_2 /perovskite/CuSCN/MoO_x (9 nm)/ITO(100 nm) /Au. The structure can harvest sun-light from both sides.[41] To investigate the effect of F4TCNQ doping on charge collection in ST-PSCs, the J–V curves of ST-PSCs with illumination from CuSCN and ITO/glass sides are shown in Figs. 5(c) and 5(d), and Table 2 also lists the corresponding detailed parameters. The parameters of bifacial semitransparent device with doped CuSCN indicate a V_{oc} of 1.06 V, a J_{SC} of 20.4 mA/cm^2, a fill factor of 68% and a PCE of 14.8% by illuminating from ITO side, and a V_{oc} of 1.02 V, a J_{SC} of 19.2 mA/cm^2, an FF of 64% and a PCE of 12.5% by illuminating from doped CuSCN side. The corresponding EQE of PSCs is shown in Figs. 5(e) and 5(f). Compared with the undoped CuSCN device, the semi-transparent device with doped CuSCN exhibits higher PCE and external quantum efficiency values in the range from 300 nm to 800 nm.

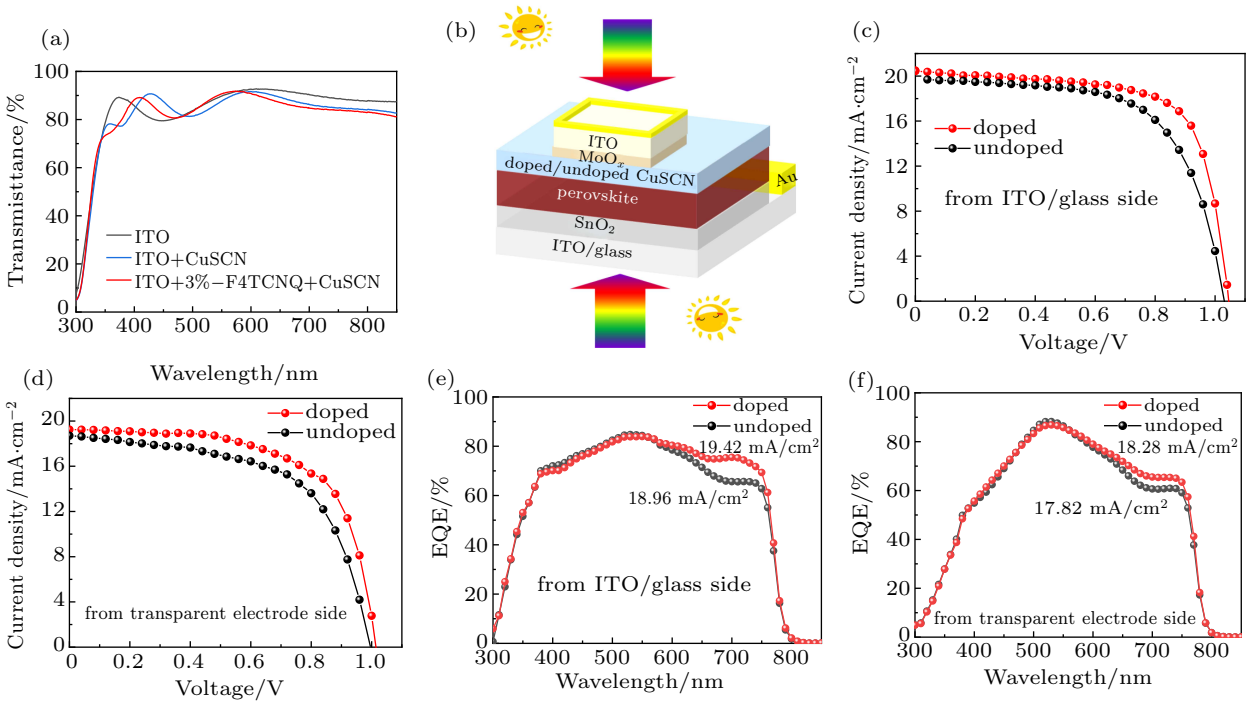


Fig. 5. (a) Transmittance spectra of a bare ITO/glass substrate, ITO-glass/undoped CuSCN substrate, and ITO-glass/doped CuSCN substrate, respectively; (b) ST-PSCs with two illumination directions. (c)–(f) *J*–*V* measurements and EQE spectra of the ST-PSCs with illumination incident from ITO/glass and transparent electrode side, respectively. The integrated J_{sc} for both sides are given in the legend.

Table 2. The *J*–*V* parameters for ST-PSCs with light incident from ITO/glass and transparent electrode side, respectively.

Sample	Light incident direction	Devices scan direction	J_{sc}[EQE] /(mA/cm^2)	J_{sc} /(mA/cm^2)	V_{oc}/V	FF/%	PCE/%
Undoped CuSCN	incident from ITO/glass side	reverse	18.84	19.9	1.02	54.7	11.1
		forward		19.7	1.02	64.2	12.9
	incident from transparent electrode side	reverse	17.82	18.9	0.98	54.1	10.1
		forward		18.7	0.98	60.1	11.1
Doped CuSCN	Incident from ITO/glass side	Reverse	19.42	20.5	1.02	68.1	14.3
		forward		20.4	1.06	68.0	14.8
	incident from transparent electrode side	reverse	18.24	19.4	1.02	58.9	11.6
		forward		19.2	1.02	63.6	12.5

4. Conclusion

In summary, a molecular doping strategy is used to tailor the electronic properties of inorganic CuSCN hole transporting layer. The doped CuSCN has a superior conductivity and well-matched energy level with perovskite, which is beneficial for hole transferring from perovskite to doped CuSCN and reducing the recombination at perovskite/CuSCN interface. As a result, the champion opaque cells with doped CuSCN exhibits PCE of 16.6%, J_{sc} of 21.5 mA/cm^2, V_{oc} of 1.10 V, FF of 70.5%. When employing as HTM in bifacial semitransparent n–i–p planar PSCs, the maximum efficiency of 14.8% and 12.5% are achieved by illuminating from the front side and rear side, respectively. This work can be used for reference to improve the efficiency of ST-PSCs based on CuSCN and will promote the development of BIPV.

Appendix A: Supporting information

Some measurement results for undoped CuSCN and doped CuSCN are shown in the following figures and tables.

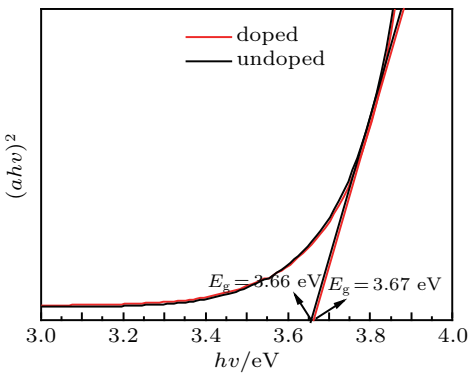


Fig. A1. The relationship between $(\alpha hv)^2$ and energy of CuSCN and 3% F4TCNQ-doped CuSCN film. The band gap can be determined by tangent of the curve to the base line. It can be found that the band gaps of the CuSCN and 3% F4TCNQ-doped CuSCN are about 3.66 eV and 3.67 eV.

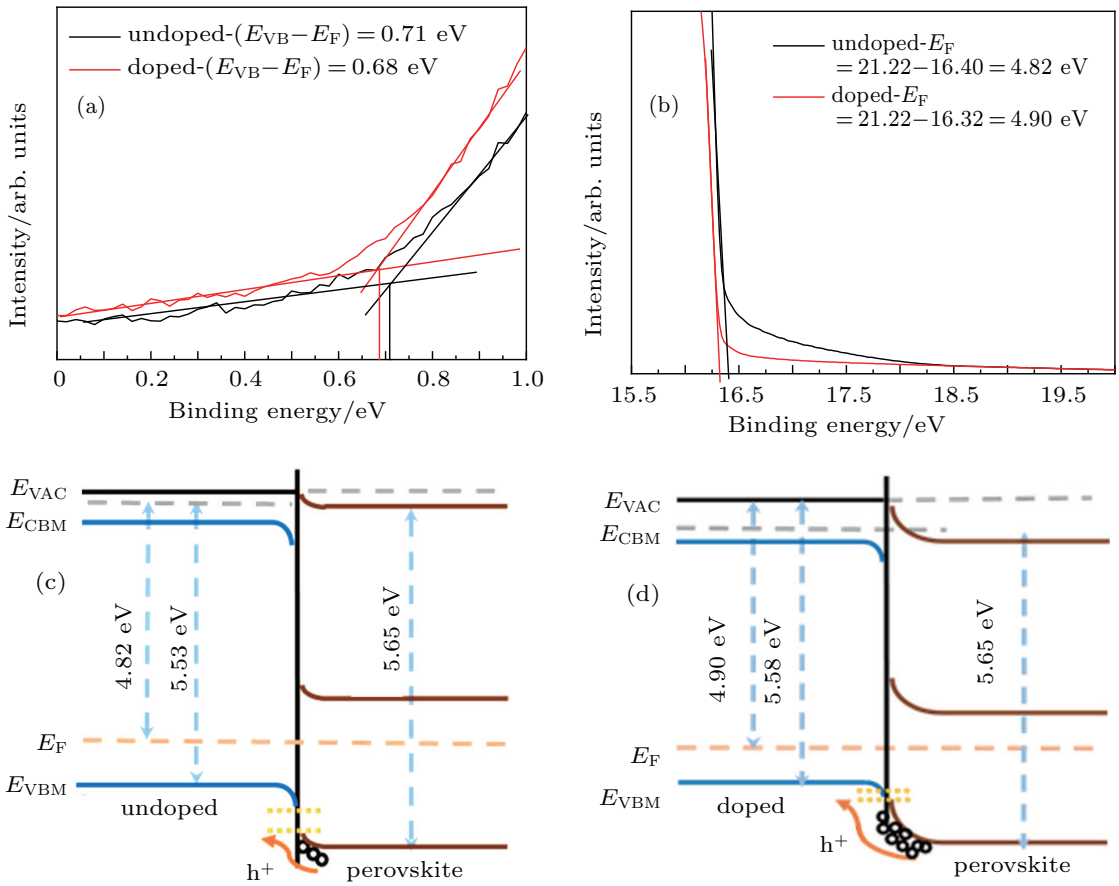


Fig. A2. (a) Valance band spectra of the CuSCN and F4TCNQ-doped CuSCN. (b) UPS spectra of the CuSCN and F4TCNQ-doped CuSCN, measured under −21.22-eV bias. Band bending at CuSCN-perovskite interface of before (c) and after (d) doping F4TCNQ.

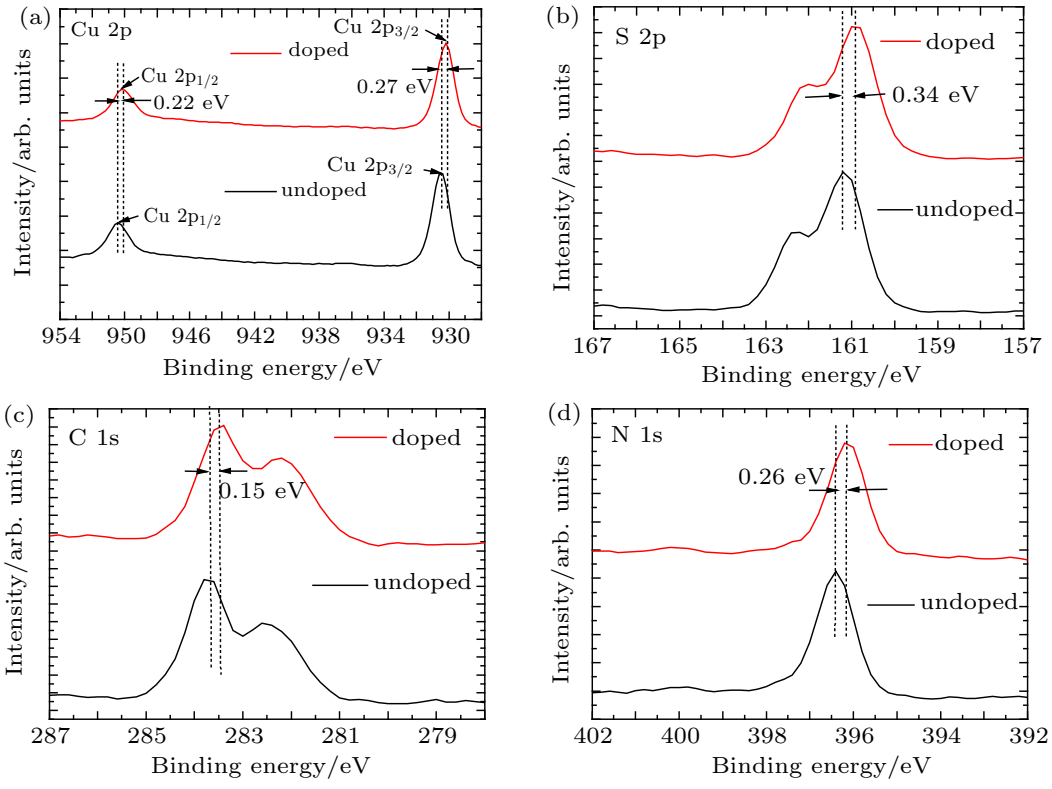


Fig. A3. XPS spectra of CuSCN and F4TCNQ-doped CuSCN for the core level of Cu 2p (a), S 2p (b), C 1s (c), and N 1s (d); the core level of Cu $2p_{1/2}$ shifted ≈ 0.22 eV and Cu $2p_{3/2}$ shifted ≈ 0.27 eV after molecular doped; the core level of S 2p shifted ≈ 0.34 eV after molecular doped; the core level of C 1s shifted ≈ 0.15 eV after molecular doped; the core level of S 2p shifted ≈ 0.26 eV after molecular doped.

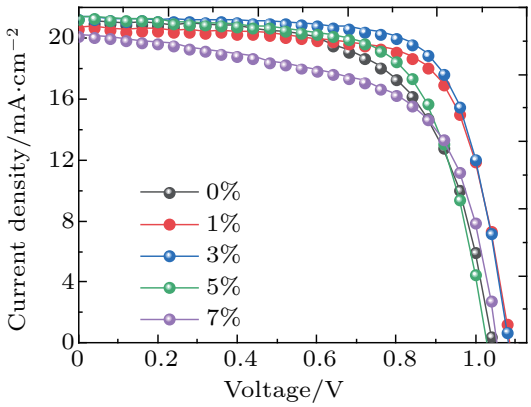


Fig. A4. Forward scan *J*–*V* curves of the optimal CsFAMA PSCs with F4TCNQ-doped CuSCN HTM under 1-sun illumination.

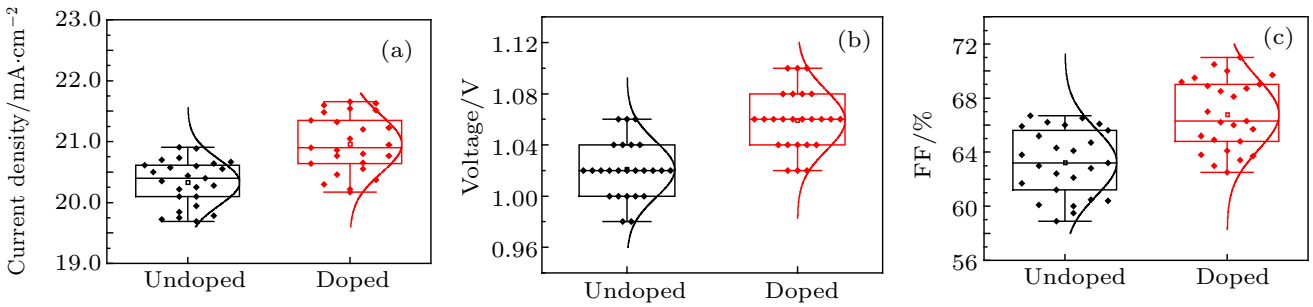


Fig. A5. Statistics of device parameters (J_{sc}, V_{oc}, and FF) for PSCs based on CuSCN or F4TCNQ-doped CuSCN HTM (25 cells are included).

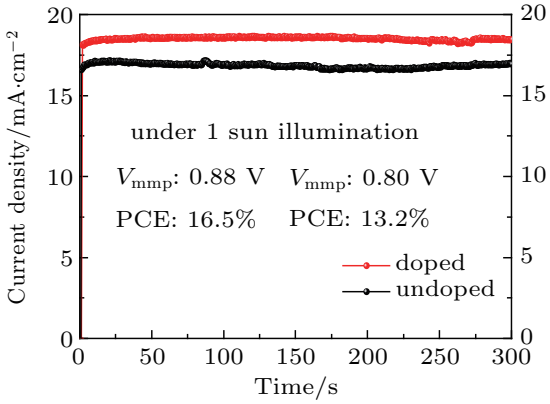


Fig. A6. Steady photocurrent output at fixed bias of V_{mpp} and steady PCE of the corresponding optimal devices.

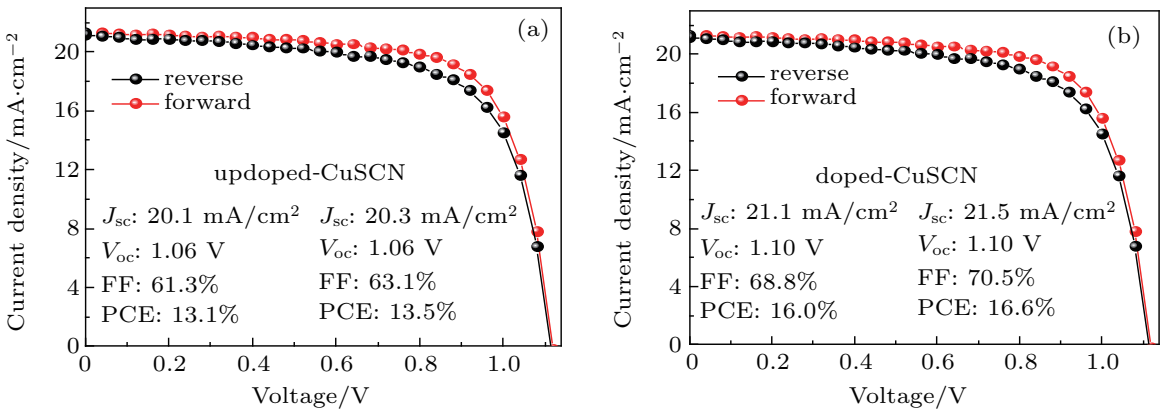


Fig. A7. Reverse and forward *J*–*V* curves of the optimal CsFAMA PSCs using (a) CuSCN and (b) F4TCNQ-doped CuSCN as HTMs under 1-sun illumination.

Table A1. Summary of the carrier lifetime from fitting curves of the TRPL measurements.

Sample	τ_1/ns	A_1/%	τ_2/ns	A_2/%
Glass/CsFAMA/undoped CuSCN	39.68	7.74	213.49	92.26
Glass/CsFAMA/doped CuSCN	25.46	3.63	328.81	96.37

Table A2. The device performance with changed F4TCNQ concentration.

HTM	Averaged J_{sc} /(mA/cm^2)	Averaged FF/V	Averaged FF/%	PCE/%	
				Average	Max
CuSCN +0% FTCNQ	20.25 ± 0.66	1.02 ± 0.04	63.2 ± 3.5	13.05 ± 0.85	13.58
CuSCN +1% F4TCNQ	20.52 ± 0.68	1.06 ± 0.04	64.5 ± 4.5	14.03 ± 0.96	15.88
CuSCN +3% F4TCNQ	20.86 ± 0.85	1.06 ± 0.04	65.5 ± 4.5	14.48 ± 1.11	16.61
CuSCN +5% F4TCNQ	20.44 ± 0.72	1.06 ± 0.04	63.2 ± 3.5	13.69 ± 1.02	14.57
CuSCN +7% F4TCNQ	19.85 ± 0.75	1.02 ± 0.04	60.3 ± 3.5	12.03 ± 0.88	12.66

References

[1] Cannavale A, Hörantner M, Eperon G E, Snaith H J, Fiorito F, Ayr U and Martellotta F 2017 *Appl. Energy* **194** 94

[2] Kim B J, Kim D H, Lee Y Y, Shin H W, Han G S, Hong J S, Mahmood K, Ahn T K, Joo Y C and Hong K S 2015 *Energy Environ. Sci.* **8** 916

[3] Singh P and Gupta S J J 2019 *Int. J. Sci. Tech. Advancements* **5** 33

[4] Köhnen E, Jošt M, Morales-Vilches A B, Tockhorn P, Al-Ashouri A, Macco B, Kegelmann L, Korte L, Rech B and Schlatmann R 2019 *Sustainable Energy Fuels* **3** 1995

[5] Hanmandlu C, Chen C Y, Boopathi K M, Lin H W, Lai C S and Chu C W 2017 *ACS. Appl. Mater. Interfaces* **9** 32635

[6] https://www.nrel.gov/

[7] Wang P Y, Li R J, Chen B B, Hou F H, Zhang J, Zhao Y and Zhang X D 2020 *Adv. Mater.* **32** 1905766

[8] Wang P Y, Jiang Q, Zhao Y, Chen Y, Chu Z, Zhang X W, Zhou Y Q and You J B 2018 *Sci. Bull.* **63** 726

[9] Li, R J, Wang P Y, Chen B B, Cui, X H, Ding Y, Li Y L, Zhang D K, Zhao Y and Zhang X D 2019 *ACS Energy Lett.* **5** 79

[10] Shi B, Duan L, Zhao Y, Luo J and Zhang X 2019 *Adv. Mater.* **32** 1806474

[11] Jeon N J, Lee H G, Kim Y C, Seo J, Noh J H, Lee J and Seok S 2014 *J. Am. Chem. Soc.* **136** 7837

[12] Luo D, Yang W, Wang Z, Sadhanala A, Hu Q, Su R, Shivanna R, Trindade G F, Watts J F and Xu Z 2018 *Science* **360** 1442

[13] Kung P K, Li M H, Lin P Y, Chiang Y H, Chan C R, Guo T F and Chen P 2018 *Adv. Mater. Interfaces* **5** 1800882

[14] Pattanasattayavong P, Yaacobi-Gross N, Zhao K, Ndjawa G O N, Li J, Yan F, O'Regan B C, Amassian A and Anthopoulos T D 2013 *Adv. Mater.* **25** 1504

[15] Arora N, Dar M I, Hinderhofer A, Pellet N, Schreiber F, Zakeeruddin S M and Grätzel M 2017 *Science* **358** 768

[16] Jung J W, Chueh C C and Jen A K Y 2015 *Adv. Energy Mater.* **5** 1500486

[17] Fan L, Li Y, Yao X, Ding Y, Zhao S, Shi B, Wei C, Zhang D, Li B and Wang G 2018 *ACS Appl. Energy Mater.* **1** 1575

[18] Wang H, Dewi H A, Koh T M, Bruno A, Mhaisalkar S G and Mathews N 2020 *ACS Appl. Mater. Interfaces* **12** 484

[19] Jin I S, Lee J H, Noh Y W, Park S H and Jung J W 2019 *Inorg. Chem. Front.* **6** 2158

[20] Wang S, Huang Z, Wang X F, Li Y M, Gunther M, Valenzuela S, Parikh P, Cabreros A, Xiong W and Meng Y S 2018 *J. Am. Chem. Soc.* **140** 16720

[21] Pellaroque A, Noel N K, Habisreutinger S N, Zhang Y D, Barlow S, Marder S and Snaith H J 2017 *ACS Energy Lett.* **2** 2044

[22] Wang Q, Bi C and Huang J 2015 *Nano Energy* **15** 275

[23] Chen W, Wu Y H, Fan J, Djurisic A B, Liu F Z, Tam H W, Ng A, Surya C, Chan W K, Wang D and He Z B 2018 *Adv. Energy Mater.* **8** 1703519

[24] Li M, Wang Z K, Yang Y G, Hu Y, Feng S L, Wang J M, Gao X Y and Liao L S 2016 *Adv. Energy Mater.* **6** 1601156

[25] Zhang Y, Elawad M, Yu Z, Jiang X, Lai J and Sun L 2016 *RSC Adv.* **6** 108888

[26] Senthilkumar N, Park S, Kang H S, Park D W and Choe Y 2011 *J. Ind. Eng. Chem.* **17** 799

[27] Zhu L, Kim E G, Yi Y and Bredas J L 2011 *Chem. Mater.* **23** 5149

[28] Su P Y, Huang L B, Liu J M, Chen Y F, Xiao L M, Kuang D B, Mayor M and Su C Y 2017 *J. Mater. Chem. A* **5** 1913

[29] Wu W Q, Wang Q, Fang Y, Shao Y, Tang S, Deng Y, Lu H, Liu Y, Li T and Yang Z 2018 *Nat. Commun.* **9** 1625

[30] Chen W, Zhou Y, Wang L, Wu Y, Tu B, Yu B, Liu F, Tam H W, Wang G and Djurišić A B 2018 *Adv. Mater.* **30** 1800515

[31] Gelmetti I, Montcada N F, Pérez-Rodríguez A, Barrena E, Ocal C, García-Benito I, Molina-Ontoria A, Martín N, Vidal-Ferran A and Palomares E 2019 *Energy Environ. Sci.* **12** 1309

[32] Fan L, Ding Y, Luo J, Shi B, Yao X, Wei C, Zhang D, Wang G, Sheng Y and Chen Y 2017 *J. Mater. Chem. A* **5** 7423

[33] Chen P, Bai Y, Wang S, Lyu M, Yun J H and Wang L 2018 *Adv. Funct. Mater.* **28** 1706923

[34] Muthu C, Agarwal S, Vijayan A, Hazra P, Jinesh K B and Nair V C 2016 *Adv. Mater. Interfaces* **3** 1600092

[35] Du Y, Xin C, Huang W, Shi B, Ding Y, Wei C, Zhao Y, Li Y and Zhang X 2018 *ACS Sustainable Chem. Eng.* **6** 16806

[36] Tang Z G, Bessho T, Awai F, Kinoshita T, Maitani M M, Jono R, Murakami T N, Wang H, Kubo T, Uchida Satoshi and Segawa H 2017 *Sci. Rep.* **7** 12183

[37] Li Z, Tinkham J, Schulz P, Yang M, Kim D H, Berry J, Sellinger A and Zhu K 2017 *Adv. Energy Mater.* **7** 1601451

[38] Liu P, Wang W, Liu S M, Yang H G and Shao Z P 2019 *Adv. Energy Mater.* **9** 1803017

[39] Li W, Dong H, Guo X, Li N, Li J, Niu G and Wang L 2014 *J. Mater. Chem. A* **2** 20105

[40] Chen W, Liu F Z, Feng X Y, Djurišić A B, Chan W K and He Z B 2017 *Adv. Energy Mater.* **7** 1700722

[41] Zhu S, Yao X, Ren Q, Zheng C, Li S, Tong Y, Shi B, Guo S, Fan L and Ren H 2018 *Nano Energy* **45** 280